PHYSICAL REVIEW B **112**, 104443 (2025)

Magnetoelastic-coupling-assisted first-order antiferromagnetic transitions in the corrugated honeycomb-lattice compounds (Ca, Sr)Mn_2P_2

Santanu Pakhira,[1,2,*] Liran Wang,[2] N. S. Sangeetha,[3] Aashish Sapkota,[4] Teslin R. Thomas,[3] Andreas Kreyssig,[3]
Frédéric Hardy,[2] Anna E. Böhmer,[3] Christoph Meingast,[2] and David C. Johnston[4,5]
[1]*Department of Physics, Maulana Azad National Institute of Technology Bhopal 462003, India*
[2]*Institute for Quantum Materials and Technologies, Karlsruhe Institute of Technology, 76131 Karlsruhe, Germany*
[3]*Experimental Physics IV, Ruhr University Bochum, 44801 Bochum, Germany*
[4]*Ames National Laboratory, Iowa State University, Ames, Iowa 50011, USA*
[5]*Department of Physics and Astronomy, Iowa State University, Ames, Iowa 50011, USA*

(Received 28 January 2025; revised 10 July 2025; accepted 3 September 2025; published 29 September 2025)

Understanding the origin of unconventional magnetic order is a central theme in the research field of functional quantum materials for spin-dependent applications. In general, a paramagnetic (PM) to antiferromagnetic (AFM) transition is of thermodynamically second order in nature in the absence of a magnetic field. In the magnetically frustrated corrugated-honeycomb lattice compounds (Ca, Sr)Mn_2P_2, electrical resistivity ρ measurements in the *ab* plane are reported to exhibit sharp discontinuities at the respective PM to AFM ordering temperatures $T_N = 69.5$ and 53 K, respectively, signifying the unusual first-order nature of the AFM transition. To reveal the origin of such anomalous transitions, high-resolution linear thermal-expansion measurements are reported for both $CaMn_2P_2$ and $SrMn_2P_2$ in the *ab* plane and along the *c* axis using capacitance dilatometry. The thermal expansion measurements show a sharp discontinuity in $\Delta L/L$ at T_N, yielding a diverging behavior in the thermal expansion coefficient $\alpha(T)$ associated with strong magnetoelastic coupling, driving the first-order AFM transition in $CaMn_2P_2$. However, this effect is weaker in $SrMn_2P_2$, consistent with the magnetic entropy changes $S(T)$ obtained from the heat-capacity measurements. Temperature-dependent *ab*-plane x-ray diffraction measurements for $CaMn_2P_2$ near its T_N yield a volume thermal expansion coefficient consistent with literature data for other materials. The uniaxial pressure derivatives of T_N in the two compounds are found to be respectively opposite in sign, presumably due to the different magnetic structures.

DOI: 10.1103/x3t1-np4q

I. INTRODUCTION

Novel functional magnetic materials comprise a modern realm of science and technology. Although ferromagnetic materials, which exhibit a spontaneous net magnetization are widely used in many technologies, the presence of stray magnetic fields and instabilities in the presence of a weak magnetic field restricts its application in many cases. In contrast, the absence of stray fields, high intrinsic precession frequency, and high stability to magnetic perturbations in antiferromagnetic (AFM) materials are quite advantageous in many spin-transport-based applications. Recently, AFM materials have gained significant interest in spintronics applications such as in spin sensors, magnetoresistive random-access memory (MRAM) devices, spin-transfer torque MRAM devices, and spin switches [1–5]. In order to verify and enhance the adaptability of functional AFM materials for spin-transport applications, it is thus of significant interest to understand the types and mechanisms of the magnetic transitions in such materials.

A paramagnetic (PM) to AFM transition in zero magnetic field is usually thermodynamically of second-order. However, AFM materials with first-order transitions in zero field can have enhanced functionality and performance in spin-transport-based applications due to the higher energy efficiency associated with the sharp change in the thermodynamic state with temperature, robustness, different AFM states, as well as faster switching speed. However, experimental realization of such materials is quite rare in nature [6–10]. Recently, two compounds $CaMn_2P_2$ and $SrMn_2P_2$ with the trigonal $CaAl_2Si_2$ structure containing corrugated Mn honeycomb layers were discovered to exhibit first-order AFM transitions associated with latent heats. In 2020, $CaMn_2P_2$ was found from electrical resistivity ρ and heat capacity C_p measurements versus temperature T to exhibit a first-order antiferromagnetic (AFM) transition at its Néel temperature $T_N = 69.5$ K [11]. Subsequently, both $CaMn_2P_2$ and $SrMn_2P_2$ were respectively found from $C_p(T)$ complemented with NMR spectroscopy measurements to exhibit strong and weak first-order transitions at their respective $T_N = 69.5$ and 53 K as shown in Fig. 1 [12]. As the number of compounds with first-order AFM transition is quite limited, it is of great interest

---

[*] Contact author: spakhira.phy@gmail.com

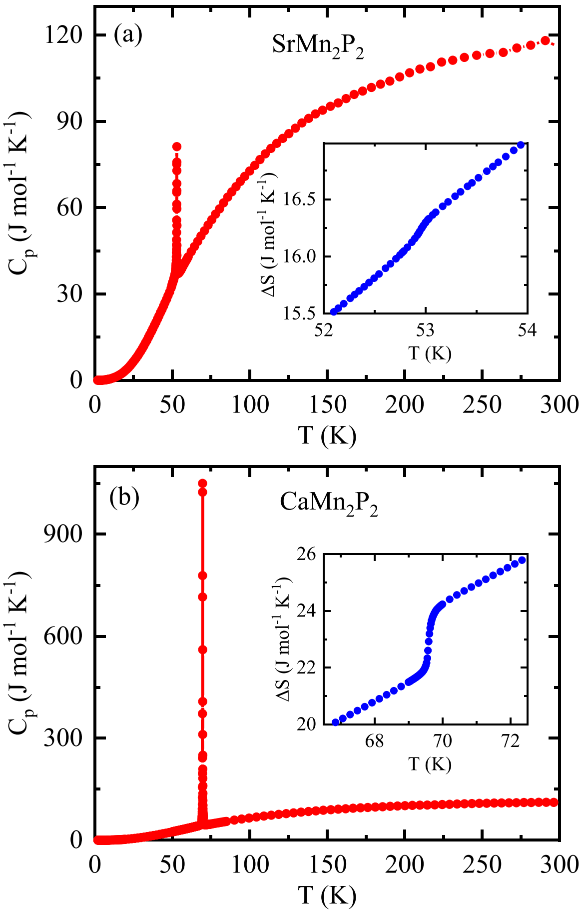

FIG. 1. Heat capacity C_p versus temperature T for (a) $SrMn_2P_2$ and (b) $CaMn_2P_2$, exhibiting first-order transitions at the associated T_N, respectively [12]. The large difference between the ordinate scales indicate that $CaMn_2P_2$ undergoes a strong first-order transition whereas $SrMn_2P_2$ exhibits a much weaker one at the respective T_N. The insets show the entropy changes (Table II) across the transition temperatures, respectively, where that for $SrMn_2P_2$ is much weaker than for $CaMn_2P_2$.

to understand the mechanism and coupling energies driving the first-order transitions in $CaMn_2P_2$ and $SrMn_2P_2$ in order to develop such materials for technological applications. Theoretical calculations and neutron-diffraction measurements indicated that the Mn spins in the Ca compound exhibit single-ion anisotropy with the emergence of Potts nematicity below T_N [13]. This insight underscores the intricate interplay of magnetic interactions and structural distortions driving the first-order AFM transitions observed in these compounds.

Here we report thermal-expansion measurements $\alpha(T)$ in the *ab* plane and along the *c* axis on $CaMn_2P_2$ and $SrMn_2P_2$ crystals using high-resolution capacitance dilatometry across their respective first-order AFM phase transitions that also covered the full temperature range from 4 K to 300 K. We also carried out volume thermal-expansion measurements using T-dependent x-ray diffraction measurements on $CaMn_2P_2$ near its T_N. In addition, we measured the changes in the resistivity $\rho(T)$ of both $CaMn_2P_2$ and $SrMn_2P_2$ at and near their respective T_N. A sharp discontinuity in the $\Delta L/L$ at T_N reveals a strong magnetoelastic coupling driving the first-order transition in $CaMn_2P_2$, whereas a smaller discontinuity signifies weaker magnetoelastic coupling in $SrMn_2P_2$, where the first-order transition is much weaker in nature. All measurements and the comparative studies are consistent with a strong first-order transition at T_N of $CaMn_2P_2$ and a weak one at T_N of $SrMn_2P_2$.

The experimental details are given in Sec. II and the *ab*-plane electrical resistivity data are presented in Sec. III. The volume thermal expansion measurements using single-crystal x-ray diffraction are shown in Sec. IV A and the linear thermal-expansion $\alpha(T)$ measurements obtained using capacitance dilatometry are presented and discussed in Sec. IV B. The temperature dependences of the Grüneisen parameters calculated from the $C_p(T)$ and $\alpha(T)$ data are presented in Sec. IV C. Concluding remarks are given in Sec. V.

II. EXPERIMENTAL DETAILS

$CaMn_2P_2$ and $SrMn_2P_2$ crystals were grown in Sn flux and characterized as described in Ref. [12]. Semiquantitative chemical analyses of the crystals were obtained using a Coxem scanning-electron microscope with an energy-dispersive x-ray detector, yielding the expected molar ratio (Ca or Sr):Mn:P = 1:2:2. The presence of Sn or other impurities in the crystals was not detected to within the instrument sensitivity.

Four-probe dc $\rho(T)$ measurements were carried out using a Keithley 2400 source meter as well as a Keithley 6221/2182A delta mode setup in a closed-cycle cryostat. Electrical contacts to a crystal were made using annealed 0.025 mm diameter Pt wires and silver paint. The dimensions of the crystals used for the measurements were 1.04 mm × 0.9 mm × 1.01 mm for $CaMn_2P_2$ and 1.1 mm × 0.4 mm × 0.5 mm for $SrMn_2P_2$.

Temperature-dependent thermal-expansion measurements were carried out between 5 K and 300 K using a home-built high-resolution capacitance dilatometer [14]. Both in-plane and *c*-axis measurements were made on crystals of typical 1–2 mm dimensions. No significant differences in the thermal expansion anomalies were observed for the two crystallographic in-plane hexagonal directions, and, therefore, the in-plane data are simply labeled as "in-plane."

To obtain additional volume thermal-expansion data, single-crystal x-ray diffraction measurements at Ames National Laboratory were performed on a four-circle diffractometer using Cu $K_{\alpha 1}$ radiation from a rotating-anode x-ray source using a germanium (1,1,1) monochromator. A He closed-cycle refrigerator was used for the temperature-dependent measurements between 11 and 300 K. Three Be domes were used as a vacuum shroud, heat shield, and the last innermost dome containing the sample, respectively. The innermost dome was filled with a small amount of He gas to improve thermal contact with the crystal surface. Measurements were carried out on a single crystal attached to a flat copper sample holder attached to the cold finger. The mosaicities of the crystal were less than 0.03° for both the (0,0,5) and (1,0,5) r.l.u. reflections at all measured temperatures. The positions of the reflections were fitted using a Lorentzian lineshape and used to determine the lattice parameters of the crystal in the temperature range from 40–90 K.

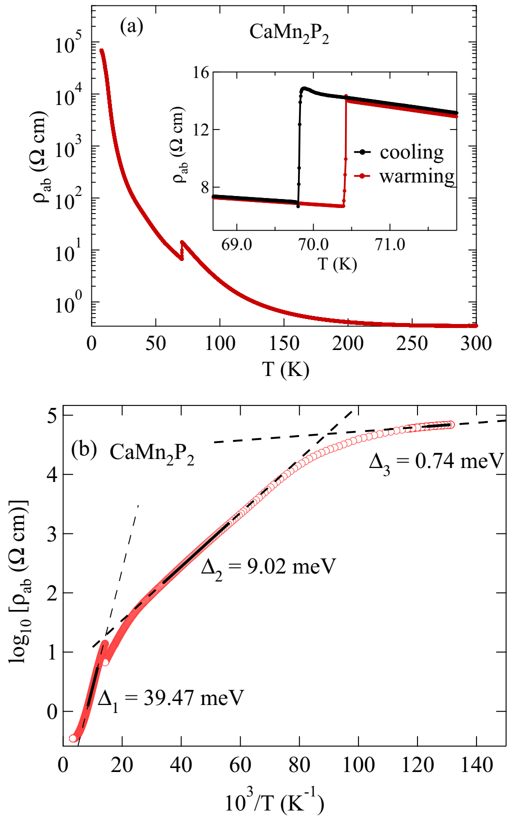

FIG. 2. (a) $\mathrm{Log}_{10}(\rho_{ab})$ of $\mathrm{CaMn_2P_2}$ versus T, indicating an insulating ground state for $T \to 0$ K. The inset shows expanded plots of the data on warming and cooling through T_{N}, where a clear hysteresis is seen as appropriate for a first-order AFM transition. (b) $\log_{10}(\rho_{ab})$ versus $10^3/T$. Three linear regions are observed, yielding the activation energies listed. The solid black lines are fits to the data and the black dashed curves are extrapolations of the fits.

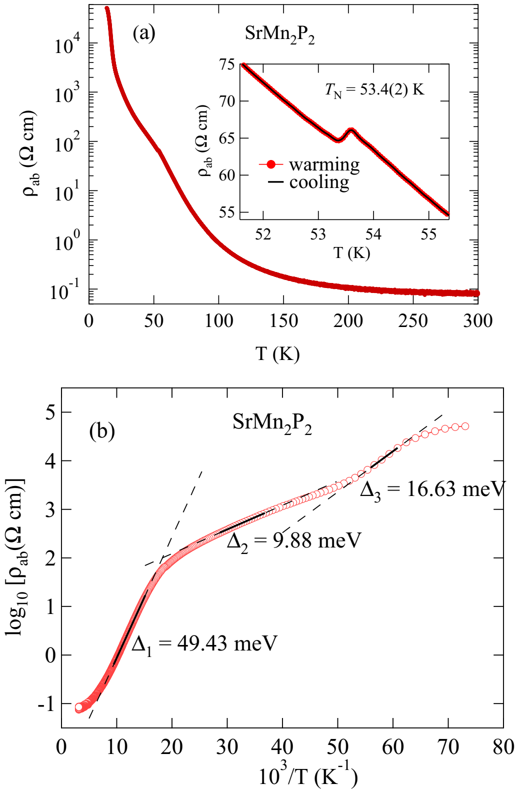

FIG. 3. (a) $\mathrm{Log}_{10}(\rho_{ab})$ of $\mathrm{SrMn_2P_2}$ versus T, indicating an insulating ground state for $T \to 0$ K. The inset shows expanded plots of the data on warming and cooling through T_{N}, where no hysteresis is observed. (b) $\log_{10}(\rho_{ab})$ versus $10^3/T$. Three linear regions are observed as indicated by solid lines, yielding the respective activation energies listed. The dashed lines are extrapolations of the fits.

III. *ab*-PLANE ELECTRICAL RESISTIVITY MEASUREMENTS

Logarithmic plots of the *ab*-plane electrical resistivity ρ_{ab} versus temperature T for $\mathrm{CaMn_2P_2}$ and $\mathrm{SrMn_2P_2}$ are shown in panels (a) of Figs. 2 and 3, respectively. These show that both compounds are insulators for $T \to 0$ K, in contrast to the semiconducting nature reported earlier for $\mathrm{SrMn_2P_2}$ [15]. Plots of $\log_{10}\rho_{ab}$ versus $10^3/T$ (K) are shown for the two compounds in Figs. 2(b) and 3(b), respectively. Each shows three linear regions with activation energies listed in the respective figures, and also listed in Table I. The intrinsic activation energy (Δ_1 at high T) of each is in the range 39–49 meV. Smaller activation energies occur at lower temperatures as listed in Table I. It is unusual to have multiple T-dependent activation energies, the origin of which remains to be resolved.

IV. THERMAL EXPANSION MEASUREMENTS

A. Single-crystal x-ray diffraction

The volume thermal expansion versus T for $\mathrm{CaMn_2P_2}$ obtained from single-crystal x-ray diffraction measurements is plotted in Figs. 4(a) and 4(b), respectively, for warming

TABLE I. Activation energies Δ obtained over restricted temperature intervals by the linear fits in Figs. 2(b) and 3(b) by $\log_{10}\rho = A + \Delta/(2.303\,k_{\mathrm{B}}T)$, where k_{B} is Boltzmann's constant.

Compound		Temperature range	Activation energy Δ (meV)
$\mathrm{CaMn_2P_2}$ [Fig. 2(b)]	Fit 1	85 K < T < 120 K	$\Delta_1 = 39.47(1)$
	Fit 2	18 K < T < 29 K	$\Delta_2 = 9.02(1)$
	Fit 3	6 K < T < 8 K	$\Delta_2 = 0.74(1)$
$\mathrm{SrMn_2P_2}$ [Fig. 3(b)]	Fit 1	65 K < T < 105 K	$\Delta_1 = 49.43(2)$
	Fit 2	27 K < T < 35 K	$\Delta_2 = 9.88(1)$
	Fit 3	16 K < T < 18 K	$\Delta_2 = 16.63(1)$

TABLE II. Entropy change (from Fig. 1) along with the uniaxial and hydrostatic pressure derivatives of T_N for $CaMn_2P_2$ and $SrMn_2P_2$.

Compound	Δ S (J/mol K)	$\frac{dT_N}{dp_a}$ (K/GPa)	$\frac{dT_N}{dp_c}$ (K/GPa)	$\frac{dT_N}{dp_{\rm hydrostatic}}$ (K/GPa)
$CaMn_2P_2$	2.17	+ 6.87	−2.13	+11.48
$SrMn_2P_2$	0.15	−1.08	+ 4.73	+2.00

and cooling cycles. The data are also compared with the volume thermal expansion estimated from thermal expansion measurements (discussed later). The average volume thermal expansion coefficient β both above and below T_N is $\beta = 2.18(6) \times 10^{-5}\ \mathrm{K}^{-1}$. The discontinuity of the unit-cell volume upon warming or cooling through $T_N = 69.0$ K reflects the first-order nature of the AFM transition. From Fig. 4(b), there is no clear difference between the values of β observed above and below T_N.

B. Capacitance dilatometry

The *ab*-plane and *c*-axis relative length changes $\Delta L/L$ and associated thermal expansion coefficients $\alpha = (1/L)dL/dT$ versus T are shown for $CaMn_2P_2$ in Figs. 5(a) and 5(b), respectively. Clear sharp first-order discontinuities are observed at $T_N = 69$ K along each direction, with opposite signs for *ab*-plane and *c*-axis directions. The volume expansion anomaly at the transition is dominated by the *ab*-plane discontinuity. Using the Clausius-Clapeyron equation

$$\frac{dT_N}{dp_i} = V_{\rm molar}\frac{\Delta L_i/L_i}{\Delta S}, \qquad (1)$$

where $V_{\rm molar}$ is the molar volume and ΔS is the change in entropy on heating through T_N, we calculate the following uniaxial and hydrostatic pressure derivatives of T_N for $CaMn_2P_2$ using the measured value of $\Delta S = 2.17$ J/mol K and the unit-cell volume of 99.88 Å^3 as

$$\frac{dT_N}{dp_a} = +6.87\ \mathrm{K/GPa},$$
$$\frac{dT_N}{dp_c} = -2.13\ \mathrm{K/GPa}, \qquad (2)$$
$$\frac{dT_N}{dp_{\rm hydrostatic}} = +11.48\ \mathrm{K/GPa}.$$

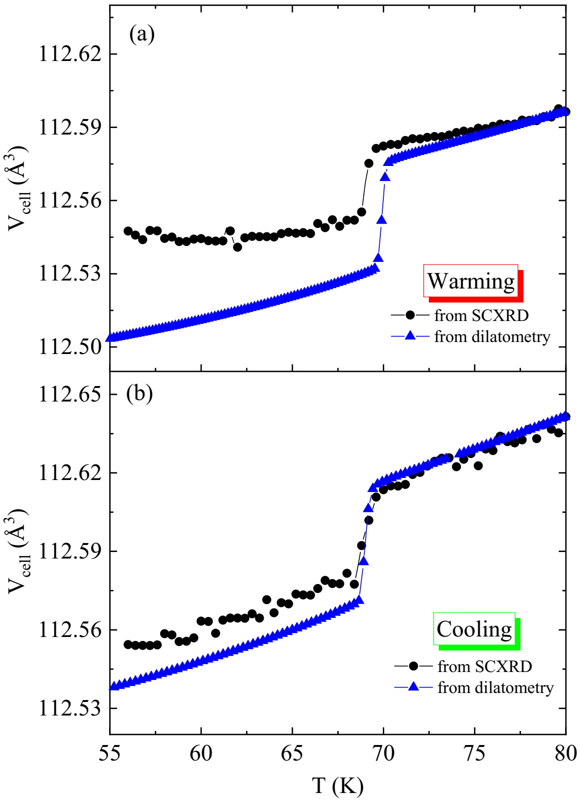

FIG. 4. A comparison of the unit cell volume $V_{\rm cell} = a^2c$ of $CaMn_2P_2$ in units of cubic angstroms versus temperature T determined using single-crystal x-ray diffraction (SCXRD) and thermal expansion measurements using capacitance dilatometry on (a) warming and (b) cooling through $T_N = 69.5$ K.

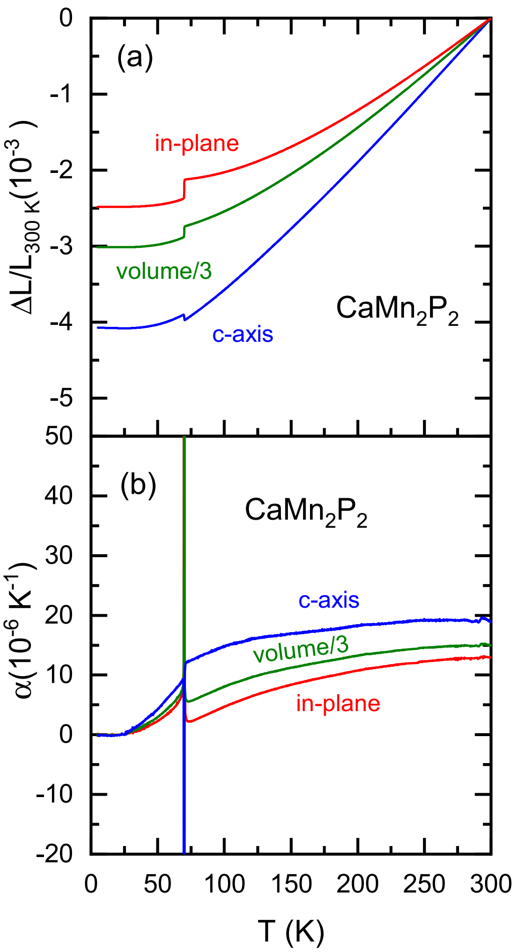

FIG. 5. (a) Change in the crystal length ΔL normalized by $L_{300\ \rm K}$ in the *ab* plane and the *c* axis versus temperature T for $CaMn_2P_2$. Also shown is the change in the volume/3 versus T. (b) Linear thermal expansion coefficient α versus temperature T for the *c* axis (blue), in the *ab* plane (red), and the volume/3 versus T (green). In (b), α in the *ab* plane at T_N increases to a value of about $600 \times 10^{-6}\ \mathrm{K}^{-1}$ (not shown).

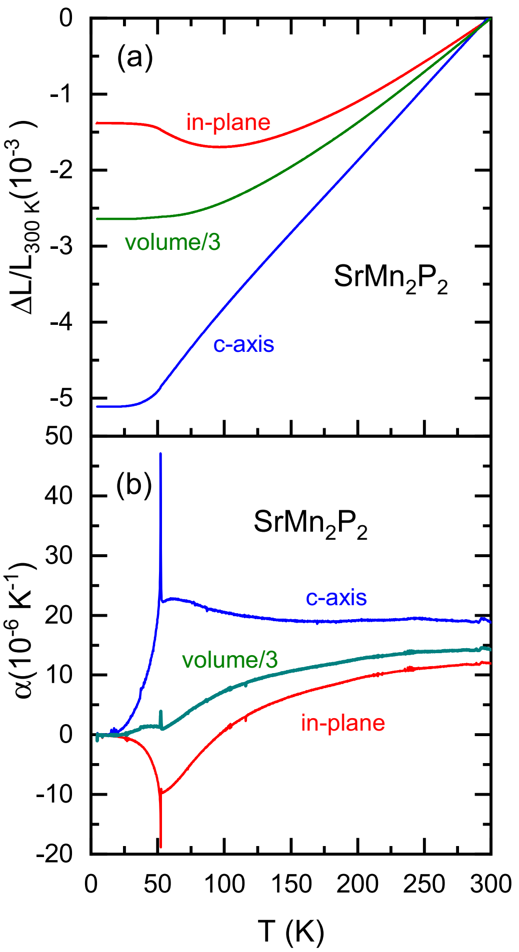

FIG. 6. (a) Change in the crystal length ΔL normalized by $L_{300\,\mathrm{K}}$ versus temperature T for $SrMn_2P_2$. (b) Linear thermal expansion coefficient α versus temperature T for the c axis (blue), the ab plane (red), and the volume/3 (green) versus T for $SrMn_2P_2$.

The obtained values are also listed in Table II. The $\Delta L/L$ and associated thermal-expansion coefficients $\alpha = (1/L)dL/dT$ of $SrMn_2P_2$ are shown in Figs. 6(a) and 6(b), respectively. In contrast to $CaMn_2P_2$, the thermal expansion of $SrMn_2P_2$ shows very weak first-order discontinuities at $T_N = 53$ K, which are only clearly visible in the $\alpha(T)$ data in Fig. 6(b). However, the thermal expansion exhibits pronounced precursor effects above T_N along both directions. These are apparently weak in the data for $CaMn_2P_2$. Again, we use these data to calculate the uniaxial and hydrostatic pressure derivatives of T_N for $SrMn_2P_2$ using $\Delta S = 0.15$ J/mol K and $V_{\mathrm{cell}} = 107.87$ Å^3, yielding

$$\frac{dT_N}{dp_a} = -1.08\ \mathrm{K/GPa},$$
$$\frac{dT_N}{dp_c} = +4.73\ \mathrm{K/GPa}, \tag{3}$$
$$\frac{dT_N}{dp_{\mathrm{hydrostatic}}} = +2.00\ \mathrm{K/GPa}.$$

The uniaxial dT_N/dp values of $SrMn_2P_2$ are of opposite sign to those of $CaMn_2P_2$ in Eq. (2), and $dT_N/dp_{\mathrm{hydrostatic}}$, although also positive, is a factor of six smaller than for $CaMn_2P_2$.

The contrasting differences in the pressure derivatives of the Néel temperature in the isostructural $CaMn_2P_2$ and $SrMn_2P_2$ can be understood from their magnetic behavior. Although the crystal structure of both compounds remains the same, the magnetic behavior of the compounds differs. In these compounds with $R\bar{3}m$ symmetry, Mn atoms from two adjacent trigonal layers are arranged in an A-B stacking pattern, creating a corrugated honeycomb structure. In the transition metal bilayer, there are no atoms between the magnetic Mn atoms, so the main interaction between nearest neighbors is likely a direct Mn-Mn coupling. The interactions between next-nearest neighbors are probably mediated by Mn-P-Mn superexchange pathways [13]. In this corrugated honeycomb structure, the nearest-neighbor (NN) exchange interaction J_1 couples two Mn ions from two adjacent trigonal layers, i.e., along the c axis, whereas, next-nearest-neighbor (NNN) exchange interaction is between the neighboring Mn ions in the same trigonal layer. The magnetic behavior of these compounds is largely controlled by the relative strength of J_1 and J_2, i.e., on the ratio J_2/J_1. Our magnetic measurements complemented with NMR studies suggested that although both $CaMn_2P_2$ and $SrMn_2P_2$ undergo AFM ordering below their respective T_Ns, the magnetic structure is commensurate for $CaMn_2P_2$, while it is incommensurate for $SrMn_2P_2$ [12]. Indeed, this prediction was further confirmed by neutron diffraction measurements for $CaMn_2P_2$, which reveals the magnetic structure consisting of in-plane 6 × 6 magnetic unit cell with a commensurate propagation vector (1/6, 1/6, L) [13]. Previous neutron diffraction studies on polycrystalline $SrMn_2P_2$ suggested a complex incommensurate magnetic structure [15], which aligns with our observations. However, the precise magnetic structure is yet to be solved. Recent theoretical calculations on $CaMn_2P_2$ reveal that the magnetic ground state is highly sensitive to the J_2/J_1 ratio. Even slight changes in this ratio can drive the system from a Néel-type collinear state to spin-spiral states with varying propagation vectors, and ultimately to a highly frustrated spin-liquid phase [16]. Not only does the nature of magnetic ordering change, but the transition temperature also changes drastically with the change in J_2/J_1 ratio. As the value of J_2/J_1 strongly depends on the NN and NNN Mn-Mn distances and the constituent elements of the compound, the magnetic interaction scenario and the associated phase diagram for $SrMn_2P_2$ is expected to be different. A comprehensive theoretical study of the magnetic phase diagram as a function of the J_2/J_1 ratio in $SrMn_2P_2$ remains an important direction for future research. It is quite plausible that the J_2/J_1 ratio evolves differently under pressure in $CaMn_2P_2$ and $SrMn_2P_2$, leading to distinct pressure-dependent behaviors of the Néel temperature in the two compounds.

The precursor effect observed in the $\alpha(T)$ above T_N can also be explained well by the magnetic behavior exhibited by the two compounds. $CaMn_2P_2$ and $SrMn_2P_2$ exhibit strong quasi-2D magnetic fluctuations above T_N, persisting up to much higher temperature as a consequence of magnetic frustration present in the systems, similar to others reported for isostructural AMn_2Pn_2 compounds (A = Ca, Sr and

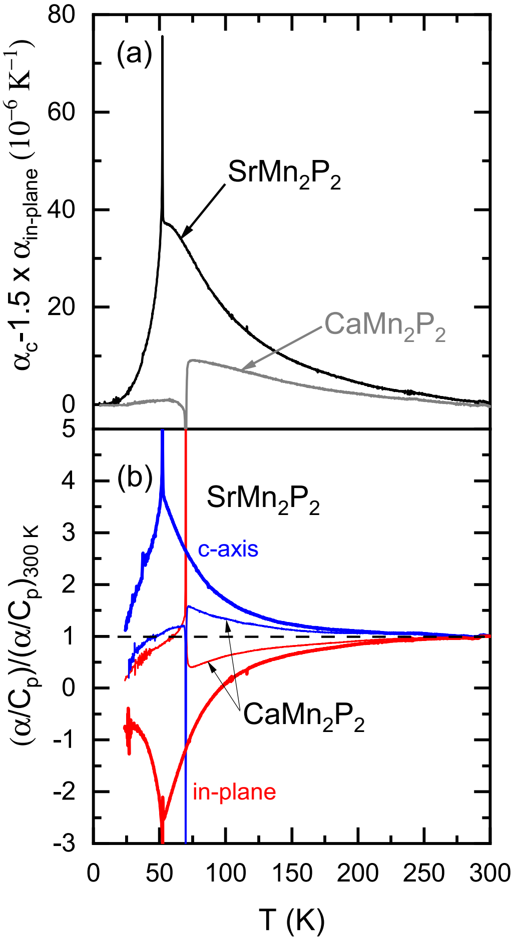

FIG. 7. (a) Difference between the c-axis thermal expansion coefficient and 1.5 times that in the *ab* plane versus temperature T. (b) T dependences of the Grüneisen parameters α/C_p for SrMn$_2$P$_2$ and CaMn$_2$P$_2$, as indicated. The data in (b) are normalized by the respective values at 300 K.

Pn = As, P, Sb) [17,18]. In these materials, hardly any sharp peak is observed at T_N in the magnetic susceptibility data, as in case of CaMn$_2$P$_2$ and SrMn$_2$P$_2$ (The anomaly due to the transition is better detected in the temperature derivative of magnetic susceptibility data) [12]. The magnetic susceptibility also does not follow Curie-Weiss behavior for $T > T_N$, where a broad hump is observed over an extended temperature range associated with the magnetic fluctuations. The effect of that precursor effect is also reflected in our thermodynamic measurements, where a broad tail is observed at higher temperatures above T_N. The effect of such magnetic fluctuations is quite prominent in the case of SrMn$_2$P$_2$, while the effect is much weaker in CaMn$_2$P$_2$, plausibly due to the much stronger spin fluctuations in SrMn$_2$P$_2$, as depicted in Fig. 7 also.

The value of $\alpha(T_N)$ for CaMn$_2$P$_2$ in Fig. 5(b) increases to 600 × 10^{-6}/K (not shown), whereas that for SrMn$_2$P$_2$ in Fig. 6(b) increases to only 48 × 10^{-6}/K. This shows that the AFM transition for CaMn$_2$P$_2$ is a strong first-order transition, whereas that for SrMn$_2$P$_2$ is a much weaker first-order transition. This large difference was also observed in the first-order heat capacity changes at T_N of CaMn$_2$P$_2$ and SrMn$_2$P$_2$ in Ref. [12].

In order to obtain a better estimate of the magnetic contribution to the thermal expansion, we plot the difference $\alpha_c - 1.5\alpha_a$ for CaMn$_2$P$_2$ and SrMn$_2$P$_2$ in Fig. 7(a). The factor of 1.5 is based on the observation that, well above the Néel temperature, the thermal expansion is dominated by nonmagnetic (primarily phononic) contributions, which exhibit the same temperature dependence along both axes [as shown in Fig. 5(b)], but with a consistently larger magnitude along the c axis. Empirically, we find that the nonmagnetic background of α_c is approximately 1.5 times that of $\alpha_{\text{in-plane}}$ in this temperature range. Thus, subtracting $\alpha_{\text{in-plane}}$ from α_c serves as a reasonable approximation to isolate the magnetic contribution to mostly eliminate the nonmagnetic background and to also enhance the magnetic signal, since the anomalies are of opposite sign for the two directions. This magnetic signal for SrMn$_2$P$_2$ has a very large contribution above its T_N, extending to roughly room temperature, and decreases rapidly below T_N. This behavior presumably results from the highly frustrated magnetism in the compound. For CaMn$_2$P$_2$, the contribution above its T_N exhibits a similar enhancement, but with a much reduced value, and the magnetic signal appears to be entirely quenched below T_N. In Fig. 7(a), the magnetic contribution to the thermal expansion, arising from fluctuations above T_N, is shown to be significantly larger in the Sr compound compared to the Ca compound. Furthermore, Fig. 7(b) reveals that the volume (or pressure) dependence of these magnetic fluctuations is also more pronounced in SrMn$_2$P$_2$ than in CaMn$_2$P$_2$. It is observed that well above the Néel temperature, the thermal expansion along both the in-plane and c-axis directions shows the same sign and a similar temperature dependence, indicating a predominantly nonmagnetic (phononic) origin. However, near the magnetic transition, the thermal expansion becomes strongly anisotropic, with the in-plane and out-of-plane components acquiring opposite signs. This sign reversal, which is absent at high temperatures, suggests a direct link to magnetic ordering and fluctuations. Additionally, the Néel temperature exhibits contrasting behavior under uniaxial pressure applied along different crystallographic directions, further supporting the anisotropic nature of the magnetic interactions.

In summary, our thermal expansion data obtained by capacitance dilatometry highlight the strong difference between the AFM transitions in SrMn$_2$P$_2$ and CaMn$_2$P$_2$. Evidence of strong magnetoelastic coupling is observed in CaMn$_2$P$_2$ whereas this coupling is weak in the case of SrMn$_2$P$_2$. CaMn$_2$P$_2$ exhibits a strong first-order transition with weak fluctuations above T_N, whereas the transition is weakly first order in SrMn$_2$P$_2$ with strong fluctuations above T_N. Although the uniaxial pressure derivatives of T_N are of opposite sign for both materials, the fluctuations above T_N interestingly have the same sign, suggesting a similar mechanism. The difference at T_N and below T_N for CaMn$_2$P$_2$ and SrMn$_2$P$_2$ are most likely related to their different magnetic structures [13,19].

C. Grüneisen parameters

The uniaxial magnetic Grüneisen parameters γ represent another method for examining the nature of the magnetic transition. The Grüneisen parameter typically measures the volume (i.e., pressure) dependence of the interactions in the system. It is defined as [20]

$$\gamma = -\partial \ln T/\partial \ln V \approx \frac{\alpha_V V K_T}{C_V}, \quad (4)$$

where α_V is the volume thermal-expansion coefficient, V is the volume, K_T is the isothermal bulk modulus, and C_V is the heat capacity at constant volume. Since changes in the bulk modulus near a magnetic phase transition are usually small, typically only a few percent, it is a reasonable approximation to treat the bulk modulus as constant when calculating the Grüneisen parameter. Ignoring the small difference between C_{V} and C_{p} in solids below 300 K and the relatively small T dependence of K_{T} and V, we utilize the expression

$$\frac{\gamma(T)}{\gamma(300\ \mathrm{K})} \approx \frac{\alpha_i(T)/C_{\mathrm{p}}(T)}{\alpha_i(300\ \mathrm{K})/C_{\mathrm{p}}(300\ \mathrm{K})} \quad (5)$$

as plotted in Fig. 7(b) for both $\mathrm{CaMn_2P_2}$ and $\mathrm{SrMn_2P_2}$, where α_i is the linear thermal expansion coefficient as above, and the $C_{\mathrm{p}}(T)$ data were obtained from Fig. 1 and the α_i data from Figs. 5(b) and 6(b), respectively.

For the Grüneisen parameter, its value at room temperature is mainly of phononic origin, as phonon Grüneisen parameters are typically small and weakly temperature dependent. Any marked enhancement at lower temperatures, particularly near T_{N}, is therefore attributed to magnetic interactions. By normalizing the temperature-dependent Grüneisen parameter to its room-temperature value, we isolate the magnetic contribution and highlight its evolution across the transition. The normalized (at 300 K) uniaxial Grüneisen parameters in Fig. 7 again exhibit strong fluctuations above the magnetic transitions, especially for $\mathrm{SrMn_2P_2}$. In contrast, for $\mathrm{CaMn_2P_2}$ the fluctuations are much weaker above T_{N}. Our data are consistent with NMR results of Ref. [12], which indicate strong 2D spin fluctuations that extend to above room temperature. For both materials, pressure or strain tuning of these fluctuations is most effective through the c/a ratio.

V. CONCLUDING REMARKS

The corrugated honeycomb-lattice insulators $\mathrm{CaMn_2P_2}$ and $\mathrm{SrMn_2P_2}$ exhibit unusual first-order AFM transitions in zero magnetic field below their respective Néel temperatures $T_{\mathrm{N}} = 69.5$ and 53 K, respectively. A sharp discontinuity is observed in the zero-field heat capacity $C_{\mathrm{p}}(T)$ and resistivity $\rho(T)$ behavior at T_{N}, associated with the first-order transition. Whereas a considerable latent heat and sizable hysteresis in $\rho(T)$ is observed for $\mathrm{CaMn_2P_2}$ at the first order transition temperature, that contribution is less for $\mathrm{SrMn_2P_2}$ because of the strong first-order nature of the AFM transition in $\mathrm{CaMn_2P_2}$ and weak one for $\mathrm{SrMn_2P_2}$. Our high-resolution linear thermal expansion $\alpha(T)$ measurements using capacitance dilatometry measurements reveal a sharp discontinuity in $\Delta L/L$ for both the *ab* plane and along the *c* axis at T_{N}, signifying the presence of strong magnetoelastic coupling assisting the first-order transition. Such coupling in $\mathrm{SrMn_2P_2}$ is rather weak as the discontinuity is smaller in $\alpha(T_{\mathrm{N}})$, resulting in a weaker first-order transition. As the first-order AFM transition in zero magnetic field is thermodynamically a rare occurrence, our results can help in understanding the mechanism of such scarce transitions in other materials. Particularly, $\mathrm{CaMn_2P_2}$ has immense potential for use in antiferromagnetic spintronics with faster switching speed. The volume thermal expansion coefficient estimated from the thermal expansion measurements agrees quite well with that obtained from temperature dependent single-crystal x-ray diffraction measurements. The estimated uniaxial pressure derivatives using the Clausius-Clapeyron equation are found to be $\frac{dT_{\mathrm{N}}}{dp_a} = +6.87$ K/GPa and -1.08 K/GPa, $\frac{dT_{\mathrm{N}}}{dp_c} = -2.13$ K/GPa and $+\,4.73$ K/GPa, and $\frac{dT_{\mathrm{N}}}{dp_{\mathrm{hydrostatic}}} = +11.48$ K/GPa and $+\,2.00$ K/GPa for $\mathrm{CaMn_2P_2}$ and $\mathrm{SrMn_2P_2}$, respectively. The AFM orderings in these compounds are quite susceptible to pressure, indicating that these compounds are promising for studying the complex interplay of lattice, spin, and electronic degrees of freedom as a function of external pressure or strain tuning.

ACKNOWLEDGMENTS

The research at Ames National Laboratory was supported by the U.S. Department of Energy, Office of Basic Energy Sciences, Division of Materials Sciences and Engineering. Ames National Laboratory is operated for the U.S. Department of Energy by Iowa State University under Contract No. DE-AC02-07CH11358. We also acknowledge support from the Deutsche Forschungsgemeinschaft (DFG) under CRC/TRR 288 (Project A02). S.P. gratefully acknowledges Dr. Ashis Kudnu, Linköping University, for valuable discussions.

DATA AVAILABILITY

The data that support the findings of this article are not publicly available upon publication because it is not technically feasible and/or the cost of preparing, depositing, and hosting the data would be prohibitive within the terms of this research project. The data are available from the authors upon reasonable request.

---

[1] V. Baltz, A. Manchon, M. Tsoi, T. Moriyama, T. Ono, and Y. Tserkovnyak, Antiferromagnetic spintronics, Rev. Mod. Phys. **90**, 015005 (2018).

[2] T. Jungwirth, X. Marti, P. Wadley, and J. Wunderlich, Antiferromagnetic spintronics, Nat. Nanotechnol. **11**, 231 (2016).

[3] T. Jungwirth, J. Sinova, A. Manchon, X. Marti, J. Wunderlich, and C. Felser, The multiple directions of antiferromagnetic spintronics, Nat. Phys. **14**, 200 (2018).

[4] H. Chen, L. Liu, X. Zhou, Z. Meng, X. Wang, Z. Duan, G. Zhao, H. Yan, P. Qin, and Z. Liu, Emerging antiferromagnets for spintronics, Adv. Mater. **36**, 2310379 (2024).

[5] S. Fukami, V. O. Lorenz, and O. Gomonay, Antiferromagnetic spintronics, J. Appl. Phys. **128**, 070401 (2020).

[6] R. Feyerherm, C. R. Wiebe, B. D. Gaulin, M. F. Collins, B. Becker, R. W. A. Hendrikx, T. J. Gortenmulder, G. J. Nieuwenhuys, and J. A. Mydosh, First-order transition to a

noncollinear antiferromagnetic structure in $U_2Rh_3Si_5$, Phys. Rev. B **56**, 13693 (1997).

[7] P. Jernberg, S. Bjarman, and R. Wäppling, $FePS_3$: A first-order phase transition in a "2D" Ising antiferromagnet, J. Magn. Magn. Mater. **46**, 178 (1984).

[8] L. Zu, S. Lin, Y. Liu, J. C. Lin, B. Yuan, X. C. Kan, P. Tong, W. H. Song, and Y. P. Sun, A first-order antiferromagnetic-paramagnetic transition induced by structural transition in $GeNCr_3$, Appl. Phys. Lett. **108**, 031906 (2016).

[9] J. M. Hastings and L. M. Corliss, First-order antiferromagnetic phase transition in MnS_2, Phys. Rev. B **14**, 1995 (1976).

[10] G. Quirion, X. Han, M. L. Plumer, and M. Poirier, First order phase transition in the frustrated triangular antiferromagnet $CsNiCl_3$, Phys. Rev. Lett. **97**, 077202 (2006).

[11] Y. J. Li, F. Jin, Z. Y. Mi, J. Guo, W. Wu, Z. H. Yu, D. S. Wu, S. H. Na, C. Mu, X. B. Zhou, Z. Li, K. Liu, L. L. Sun, Q. M. Zhang, T. Xiang, G. Li, and J. L. Luo, First-order transition in trigonal structure, Europhys. Lett. **132**, 46001 (2020).

[12] N. S. Sangeetha, S. Pakhira, Q.-P. Ding, L. Krause, H.-C. Lee, V. Smetana, A.-V. Mudring, B. Brummerstedt Iversen, Y. Furukawa, and D. C. Johnston, First-order antiferromagnetic transitions of $SrMn_2P_2$ and $CaMn_2P_2$ single crystals containing corrugated-honeycomb Mn sublattices, Proc. Nat. Acad. Sci. USA, **118**, e2108724118 (2021).

[13] F. Islam, T. V. Trevisan, T. Heitmann, S. Pakhira, S. X. M. Riberolles, N. S. Sangeetha, D. C. Johnston, P. P. Orth, and D. Vaknin, Frustrated magnetic cycloidal structure and emergent Potts nematicity in, Phys. Rev. B **107**, 054425 (2023).

[14] C. Meingast, B. Blank, H. Bürkle, B. Obst, T. Wolf, H. Wühl, V. Selvamanickam, and K. Salama, Anisotropic pressure dependence of T_c in single-crystal $YBa_2Cu_3O_7$ via thermal expansion, Phys. Rev. B **41**, 11299 (1990).

[15] S. L. Brock, J. E. Greedan, and S. M. Kauzlarich, Resistivity and magnetism of AMn_2P_2 (A = Sr, Ba): The effect of structure type on physical properties, J. Solid State Chem. **113**, 303 (1994).

[16] B. Mallick, S. Ali, and S. K. Panda, Néel order, spin-spiral, and spin liquid ground state in frustrated three dimensional system $CaMn_2P_2$: A DFT + U and spin dynamics study, Phys. Rev. B **112**, 045103 (2025).

[17] N. S. Sangeetha, A. Pandey, Z. A. Benson, and D. C. Johnston, Strong magnetic correlations to 900 K in single crystals of the trigonal antiferromagnetic insulators $SrMn_2As_2$ and $CaMn_2As_2$, Phys. Rev. B **94**, 094417 (2016).

[18] N. S. Sangeetha, V. Smetana, A.-V. Mudring, and D. C. Johnston, Antiferromagnetism in semiconducting $SrMn_2Sb_2$ and $BaMn_2Sb_2$ single crystals, Phys. Rev. B **97**, 014402 (2018).

[19] D. Vaknin, F. Islam, T. Slade, D. C. Johnston, and R. J. McQueeney, Magnetic structure of from neutron-diffraction measurements (unpublished).

[20] L. Vočadlo, J. P. Poirer, and G. D. Price, Grüneisen parameters and isothermal equations of state, Am. Mineral. **85**, 390 (2000).